nature communications

Article

https://doi.org/10.1038/s41467-025-63117-7

A templating approach with phase change to tailored coordination of single- and multiple-atom catalysts

Received: 14 May 2025

Accepted: 11 August 2025

Published online: 16 August 2025

Check for updates

Zhong-Shuai Zhu[1,5], Pengtang Wang[1,5], Haobo Li[2,5], Ya Liu[1], Yunpeng Wang[1], Kunsheng Hu[1], Bernt Johannessen[3], Shiying Ren[1], Shuang Zhong[1], Hongqi Sun[4], Xiaoguang Duan[1] ✉ & Shaobin Wang[1] ✉

Single-atom catalysts (SACs) with featured active sites exhibit exceptional catalytic activity and selectivity in catalysis. However, their scalable synthesis and precise control of structure coordination for on-demand atomic configurations remain the bottlenecks in practical applications. In this work, a facile and scalable strategy is developed to achieve massive production of varying molecular-coordinated single- and multi metal-based SACs. Low-cost NaCl is used as a recyclable and green template. Its nature of temperature-induced confinement with a phase change of ion dissociation can direct 3D honeycomb-like morphology of SACs with different coordinations of in-plane M–N_x (x = 4 or 6) at lower temperature and axial M–Cl at above melting point of NaCl (900 °C), as demonstrated by controlled experiments and theoretical computations. A library of 25 distinct SACs and high-entropy SACs containing five metals with tailored structure are synthesized in a mass yield ranging from 18.3% to 50.9%. More importantly, these SACs exhibit remarkable performance in catalytic oxidation of aqueous organics and electrocatalytic nitrate, carbon dioxide, oxygen reduction reactions, highlighting their promising potential for environmental remediation and energy applications.

Single-atom catalysts (SACs) with isolated metal atoms on supporting materials differ remarkably from traditional nanoparticle catalysts in catalytic activity[1]. Atomic-level dispersed SACs not only maximize metal utilization but also allow precise control of the chemical and electronic environment of each single metal site, thereby significantly enhancing catalytic performance[2,3]. Thus, SACs have been highly promising candidates for a range of catalytic applications, including catalytic water treatment and disinfection as well as green synthesis (e.g., NO_3^- and CO_2 reduction reactions)[4–8]. However, the practical applicability of SACs is largely contingent upon the precise and controlled large-scale synthesis strategies tailored to different catalytic reactions. One major bottleneck is the absence of a universal principle for scalable SAC synthesis to achieve repeatable, well-defined and tailored coordination using a standardized method[9,10]. Additionally, the mechanisms governing SAC formation and structural evolution remain poorly understood. The natural tendency of metal atoms to aggregate in the synthesis, driven by the Gibbs-Thomson effect[11], further challenges preservation of the atomically dispersed metal sites in deliberate synthesis.

Conventional "top-down" or "bottom-up" synthesis strategies have been explored to address these challenges[12]. Top-down methods typically involve disrupting metal-metal bonds in nanoparticles or bulk metals through physical or chemical processes (e.g., etching or mechanical milling), controlled release of metal atoms to be

[1]School of Chemical Engineering, The University of Adelaide, Adelaide, SA, Australia. [2]School of Chemistry, Chemical Engineering and Biotechnology, Nanyang Technological University, Singapore, Singapore. [3]Australian Synchrotron, ANSTO, Clayton, VIC, Australia. [4]School of Molecular Sciences, The University of Western Australia, Perth, WA, Australia. [5]These authors contributed equally: Zhong-Shuai Zhu, Pengtang Wang, Haobo Li.
✉e-mail: xiaoguang.duan@adelaide.edu.au; shaobin.wang@adelaide.edu.au

subsequently incorporated into the defects or vacancies of a supporting matrix[13,14]. However, control of defects with on-demand population and geometric features is difficult, resulting in suboptimal regulation of both metal atom dispersion and coordination environments. Conversely, bottom-up methods, where catalysts are assembled at the molecular or atomic scale followed by thermal conversion, have recently been extended to construct libraries of single-atom sites[2,9,10,15,16]. However, these approaches are often constrained by limited structural tunability and poor morphology regulation (Fig. 1a). Thus, templating strategies (e.g., SiO_2, polystyrene, and MgO) have been introduced to provide a scaffold for enhanced atomic dispersion and morphology control[17–20]. For example, Wang and co-workers used different types of SiO_2 hard template to fabricate a family of SACs (Ni, Co, Mn, Zn, Cu, Sc and Fe) with different mesoporous structures[21]. Although these template-assisted techniques achieved the SAC synthesis, challenges still remain in precisely controlling the local coordination environment of metal atoms due to the chemical inertness of the templates (Fig. 1a). Moreover, these used templates are typically non-recoverable, requiring complex and destructive removal processes that increase the costs of material synthesis and induce potential environmental risks[22]. Therefore, developing a universal and cost-saving synthesis strategy to manage large-scale SAC production with simultaneous control of morphology and coordination structure is highly desirable.

In this work, we present a versatile template-assisted strategy for massive production of a well-defined SAC library. Unlike traditional methods relying on expensive precursors/templates or unsustainable procedures, we use low-cost and recyclable NaCl as a template to simultaneously control both morphology and local coordination structure of SACs. Specifically, NaCl lattice confines metal atom migration during high-temperature pyrolysis, effectively preventing aggregation and promoting formation of a 3D honeycomb-like morphology in symmetric coordination. In addition, its ion dissociation upon melting facilitates formation of axial metal–Cl bond (Fig. 1a) for asymmetric coordination. Such pyrolysis-regulated local coordination evolution was experimentally and theoretically proved via

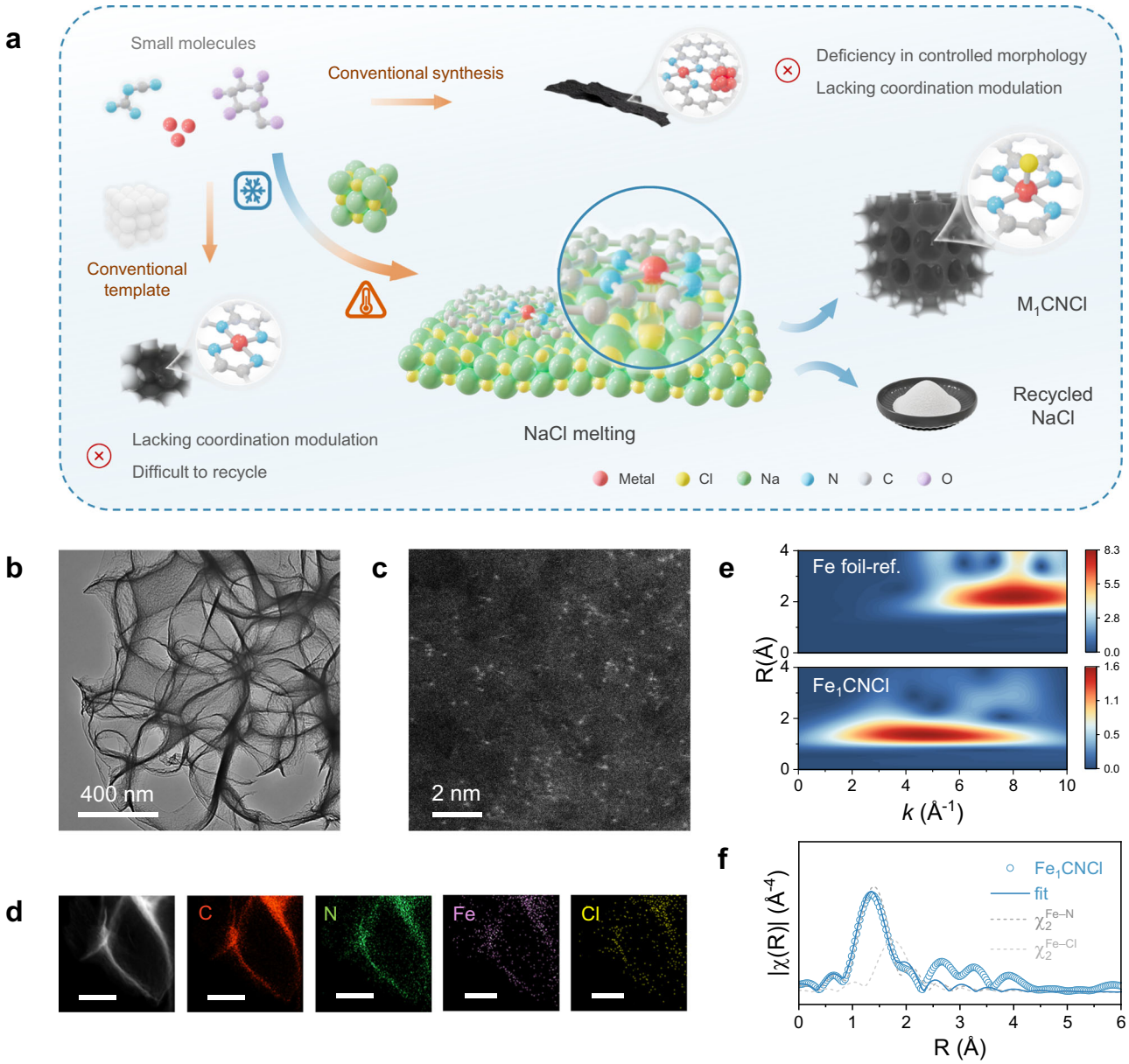

Fig. 1 | Synthesis of Fe_1CNCl. a Synthesis scheme of Fe_1CNCl. **b** TEM and **c** HAADF-STEM images of Fe_1CNCl and **d** the corresponding EDS mappings of C, N, Fe and Cl (The scale bar is 100 nm). **e** Fe K-edge WT-EXAFS plots of Fe foil and Fe_1CNCl. **f** FT-EXAFS analysis of Fe_1CNCl in R space.

temperature-dependent formation of a group of Fe SACs. Based on this strategy, we successfully synthesized a library of 25 SACs (denoted as M_1CNCl, M is corresponding metal elements) with an average mass yield of 30.5%, and multi-atom five-metal high-entropy SACs (HESACs). These designated SACs exhibited remarkable performances in catalytically activating peroxymonosulfate (PMS) to mediate a selective nonradical pathway for diverse organics oxidation in water. Additionally, the SACs also demonstrated exceptional high activity in electrocatalysis, including NO_3^- reduction, CO_2 reduction, and oxygen reduction reactions. This study not only presents a general synthetic strategy for the large-scale production of SACs with a well-defined coordination structure and 3D porous morphology but also highlights their practical potential in ensuring water safety and energy conversion.

Results

Synthesis and morphology of Fe_1CNCl

We employed a simple NaCl-templating method to successfully synthesize a series of SACs anchored on a three-dimensional (3D) nitrogen-doped porous carbon network. Taking Fe element as an illustrative example, the synthesis process and mechanism are illustrated in Fig. 1a. Initially, $FeCl_2{\cdot}4H_2O$ (Fe source), dicyandiamide (nitrogen source), glucose (carbon precursor), and sodium chloride (NaCl, hard template) were dissolved in water to form a homogeneous precursor solution. The solution was then freeze-dried to obtain a solid powder. During the freeze-drying process, cubic NaCl crystals precipitated from the solution and created a 3D hard template as water sublimated, confining the metal precursor Fe and other organic molecules (e.g., glucose and dicyandiamide) between the NaCl crystal lattices. The resulting powder mixture was then annealed at 900 °C under an argon atmosphere. During this process, glucose underwent carbonization and NaCl melted at the high temperature, which resulted in a graphitic network within the molten NaCl and evolution into a 3D Fe single-atom-dispersed nanosheet/NaCl composite. Notably, the melting-induced expansion of NaCl crystals promoted the interpenetration of carbon nanosheets, particularly at the grain boundaries of NaCl particles. Additionally, the controlled carbonization between NaCl particles ensured a high mass yield and uniformity in the carbon layers. After acid washing, the NaCl template was removed, yielding a 3D honeycomb-like structure (denoted as Fe_1CNCl).

Scanning electron microscopy (SEM) and transmission electron microscopy (TEM) images both reveal the uniformly distributed open pores (~0.5–1 μm in diameter) and the absence of large metal particles (Fig. 1b and Supplementary Fig. 1), which is confirmed by powder X-ray diffraction (XRD) (Supplementary Fig. 2). High-resolution high-angle annular dark field scanning TEM (HAADF-STEM) images display evenly dispersed bright white spots across the carbon substrate (Fig. 1c), which correspond to atomically dispersed Fe sites. Energy-dispersive X-ray spectroscopy (EDS) mapping further confirms the uniform distribution of C, N, Fe, and Cl elements in Fe_1CNCl nanosheets (Fig. 1d). Furthermore, unlike conventional templating methods, where the template is often non-recoverable or requires complex recovery processes, our method allows for the efficient recovery of the NaCl template with a recovery rate of up to 90.2% (Supplementary Fig. 3). This high recovery rate demonstrates the sustainability and cost-effectiveness of the NaCl-assisted synthesis process.

The chemical environments in Fe_1CNCl are examined using X-ray photoelectron spectroscopy (XPS) and X-ray absorption spectroscopy (XAS) techniques. As shown in Supplementary Fig. 4, the XAS absorption edge of Fe_1CNCl shows a close location to Fe_2O_3, indicating that the average valence state of Fe species in Fe_1CNCl is Fe^{3+}. The N K-edge X-ray absorption near-edge structure (XANES) spectra of the Fe_1CNCl catalysts display three well-resolved peaks, corresponding to pyridinic, pyrrolic, and graphitic N species (Supplementary Fig. 5). This finding is further supported by the high-resolution N *1 s* XPS spectra, which exhibit a Fe–N peak at 399.0 eV, indicative of FeN_x species, suggesting a distinct nitrogen environment compared to the catalyst without Fe (denoted as CN) (Supplementary Fig. 6)[23,24]. Notably, Cl *2p* spectra also confirm the Fe–Cl bond at around 198 eV in Fe_1CNCl (Supplementary Fig. 7)[23,25], indicating that both N and Cl atoms are coordinated with Fe. This arrangement diverges from the conventional pyrolysis-derived $Fe–N_4$ structures[26,27], demonstrating that our synthesis method effectively tailors the Fe coordination microenvironment.

To further elucidate the coordination environment, we conducted extended X-ray absorption fine structure (EXAFS) analysis. The wavelet transform (WT) signal of Fe_1CNCl was markedly different from the intensive WT signal of Fe foil (Fig. 1e). Consistently, the characteristic Fe–Fe coordination path at 2.2 Å in the Fourier transform (FT) EXAFS spectrum of Fe foil was absent in Fe_1CNCl (Supplementary Fig. 8). All these findings collectively suggested the absence of Fe–Fe bonds in Fe_1CNCl, confirming the atomic dispersion of Fe atoms in the Fe_1CNCl structure. To elucidate the local coordination structure of Fe_1CNCl, we further conducted a quantitative EXAFS fitting analysis (Supplementary Fig. 8). As shown in Fig. 1f and Supplementary Table 1, the best-fit model for Fe_1CNCl included two coordination paths: Fe–N and Fe–Cl. Moreover, the fitting results revealed coordination numbers of 4.3 for Fe–N and 1.0 for Fe–Cl, with bond distances of 1.91 and 2.26 Å in Fe_1CNCl, respectively. Therefore, all the analyses demonstrated the successful synthesis of atomically dispersed $Cl_1–Fe–N_4$ active sites in Fe_1CNCl.

Temperature-dependent coordination evolution of Fe SACs on the template phase

To reveal the role of the NaCl template in facilitating Fe_1CNCl formation, we performed comparative experiments without adding NaCl (denoted as Fe_1CN-woNaCl). In the absence of NaCl, a compact and minimal porous structure is observed (Supplementary Fig. 9), underscoring the importance of the NaCl template in directing the synthesis of 3D honeycomb-like morphology. Accordingly, we further investigated the temperature-dependent morphology and local structure evolution during SAC synthesis using NaCl as the template. As shown in Fig. 2a, with the pyrolysis temperature increasing from 300 to 700 °C, the resulting products (denoted as Fe_1CN-300, Fe_1CN-500 and Fe_1CN-700) exhibit pronounced changes in morphology. The morphology of Fe_1CN-300 remains amorphous due to incomplete carbonization, and the NaCl template is insufficient for structural guidance at 300 °C. However, with the increasing temperature to 500 and 700 °C, a distinct sheet-like morphology emerges for Fe_1CN-500 and Fe_1CN-700 with a higher carbonization degree, revealing that the higher temperatures enable the NaCl template to more effectively direct a stable and porous carbon framework. Notably, no bigger nanoparticle aggregate is observed under any pyrolysis temperature, which is consistent with XRD patterns (Supplementary Fig. 10). Meanwhile, HAADF-STEM images exhibit the single-atom dispersion of Fe in all samples (Fig. 2b), indicating that the NaCl template directs the universal formation of single-atom Fe sites. Likewise, the NaCl-induced morphology-guiding effect was also observed in Co and Ni systems (Supplementary Fig. 11).

We further characterized the coordination structures formed at various temperatures, focusing on the transition between different Fe–N coordination modes across the temperature range. As shown in Supplementary Fig. 12, the first derivatives XANES of Fe K-edge energy profiles of Fe_1CN-300, Fe_1CN-500 and Fe_1CN-700 show that the oxidation state of atomic Fe center gradually increases with the temperature, which can be attributed to the differing local coordination environment of the Fe single-atom sites. In addition, the FT-EXAFS results demonstrate that atomically dispersed Fe in Fe_1CN-300, Fe_1CN-500, and Fe_1CN-700 exhibits a prominent peak at ~1.60–1.47 Å, which is assigned to the Fe–N scattering path. Notably, no peak corresponding to the Fe–Fe scattering path is observed (Fig. 2c), confirming that all Fe

https://doi.org/10.1038/s41467-025-63117-7

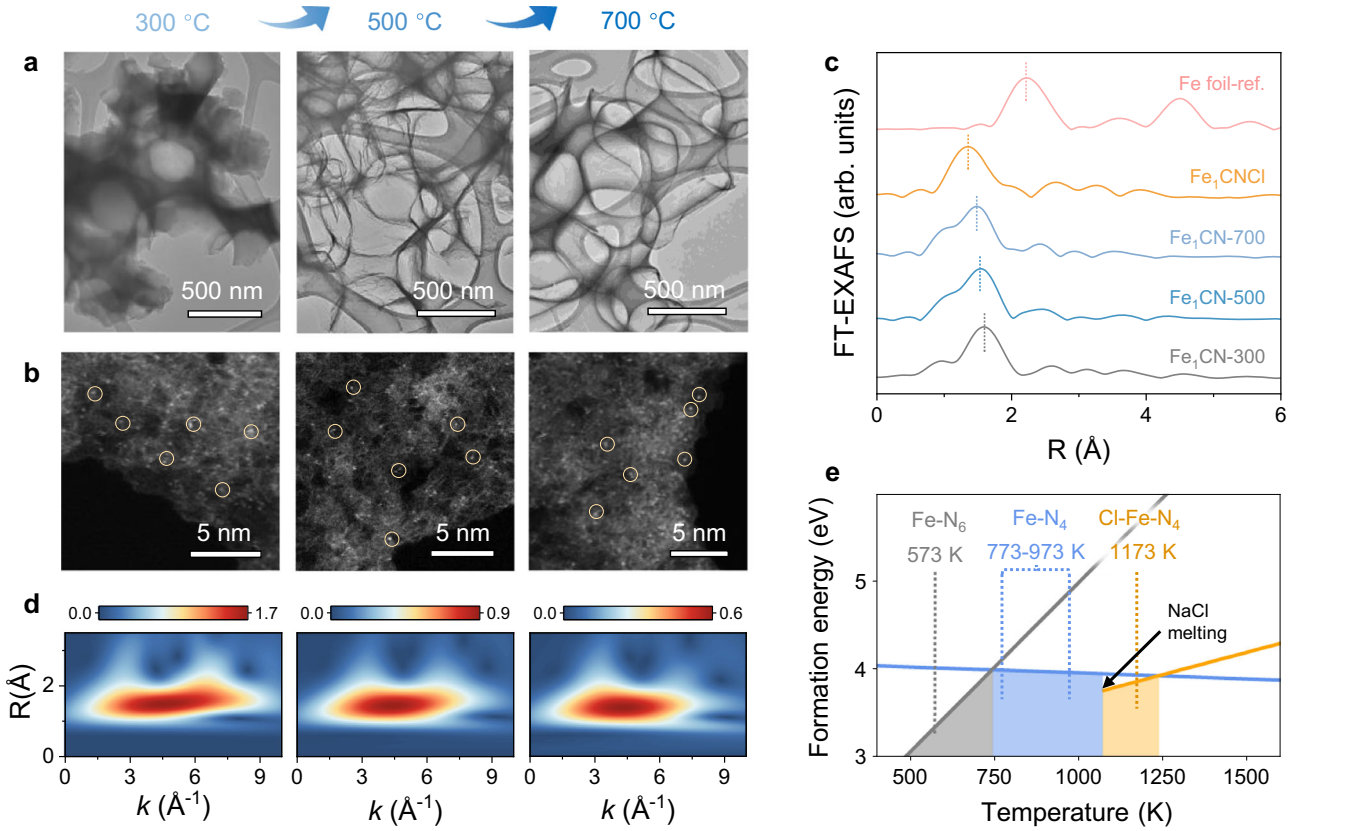

Fig. 2 | Fe SAC Formation mechanism investigation. Series of **a** TEM and **b** HAADF-STEM images of Fe SACs acquired at different temperatures. **c** EXAFS analysis of Fe SACs acquired at different temperatures. The y-axis values for each sample were individually normalized by the intensities of their respective main peaks for comparing the location of main peaks. **d** Fe K-edge WT-EXAFS plots of Fe SACs acquired at different temperatures. **e** Density functional theory calculations for formation energy of Fe SACs as a function of the temperature. The colored areas show the region of most stable structures under the lines with the lowest formation energy. The corresponding experimental temperature range is marked by dashed lines. The black arrow indicates the template activation temperature of 801 °C, beyond which Cl-containing species begin to form.

atoms in these three samples remain in isolated dispersion after pyrolysis. Furthermore, the quantitative EXAFS curve fitting reveals that, in contrast to Fe_1CNCl (synthesized at 900 °C) exhibiting an Fe–Cl scattering path, only Fe–N scattering paths can be fitted in these three samples. The corresponding Fe–N coordination numbers for Fe_1CN-300, Fe_1CN-500 and Fe_1CN-700 are 6.0, 3.9, and 3.6, respectively (Supplementary Fig. 13 and Table 1). Thus, EXAFS analyses reveal pyrolysis temperature-dependent Fe coordination structures. Specifically, at a low temperature of 300 °C, the Fe center predominantly forms the Fe–N_6 coordination. As the temperature increases to the range of 500–700 °C, the coordination number decreases, transitioning to an Fe–N_4 structure. Further, when the temperature reaches 900 °C, the coordination structure evolves into asymmetric Cl_1–Fe–N_4 with the axial incorporation of Cl_1–Fe bond. Such a temperature-dependent structural transformation can further be clearly corroborated by the WT analysis (Fig. 2d), where the shifts in the intensity maxima align with the changes in the coordination environment of the single-atom Fe sites. The above results indicate that a heat treatment at 900 °C is essential for the formation of Cl_1–Fe–N_4 configuration. Since NaCl melts at above 801 °C and dissociates into free-moving ions, we speculate that this temperature-induced Fe–Cl formation may be related to the molten state of NaCl. More specifically, at temperatures above 900 °C, molten NaCl increases chloride ion mobility, thereby promoting their interaction with dispersed iron atoms[25].

Density functional theory (DFT) calculations were conducted to examine the dependence of the Fe coordination evolution pathways on pyrolysis temperature. The stability of each structure is represented by its formation energy, incorporating temperature effects through the entropy corrections in the vibrational analysis for gas-phase molecules (Supplementary Fig. 14). As shown in Fig. 2e, at a relatively lower temperature of 573 K (300 °C), Fe tends to form a Fe–N_6 coordination. However, when the temperature increases to 773 K (500 °C), the coordination N number decreases to 4 (Fe–N_4). This Fe–N_4 remains most stable up to 1074 K (801 °C), where the NaCl template begins to melt. Beyond this temperature, molten NaCl facilitates ionic interactions with the carbon substrate and drives the formation of Cl_1–Fe–N_4 (with Cl in the axial position) at 1173 K (900 °C). These theoretical computations correspond well with the experimental results of coordination structure evolution under different temperatures (from 300 to 900 °C, Supplementary Fig. 13 and Table 1). Consequently, NaCl not only serves as a hard template to create the 3D honeycomb-like structure morphology but also promotes the formation of axial Fe–Cl coordination at high temperatures above its melting point of 801 °C.

The generality of NaCl templating synthesis

Building on the successful synthesis of Fe-based SACs, we extended the NaCl-template strategy to a wide range of metal elements to confirm its versatility and broad applicability. By simply replacing $FeCl_2{\cdot}4H_2O$ with other metal chlorides or nitrates, we produced a comprehensive library of SACs (M_1CNCl, where M represents different metal elements in Fig. 3a). This library encompasses 25 metals, spanning main group (Mg, Al, K, Ca, Ga, Ge, In, Sn, Sb, Cs, Ba, Pb, Bi), transition (Cr, Mn, Fe, Co, Ni, Cu, Zn, Cd), and rare earth metals (Y, La, Pr, Tb). In every case, each SAC exhibits a honeycomb-like porous structure under the guidance of NaCl.

https://doi.org/10.1038/s41467-025-63117-7

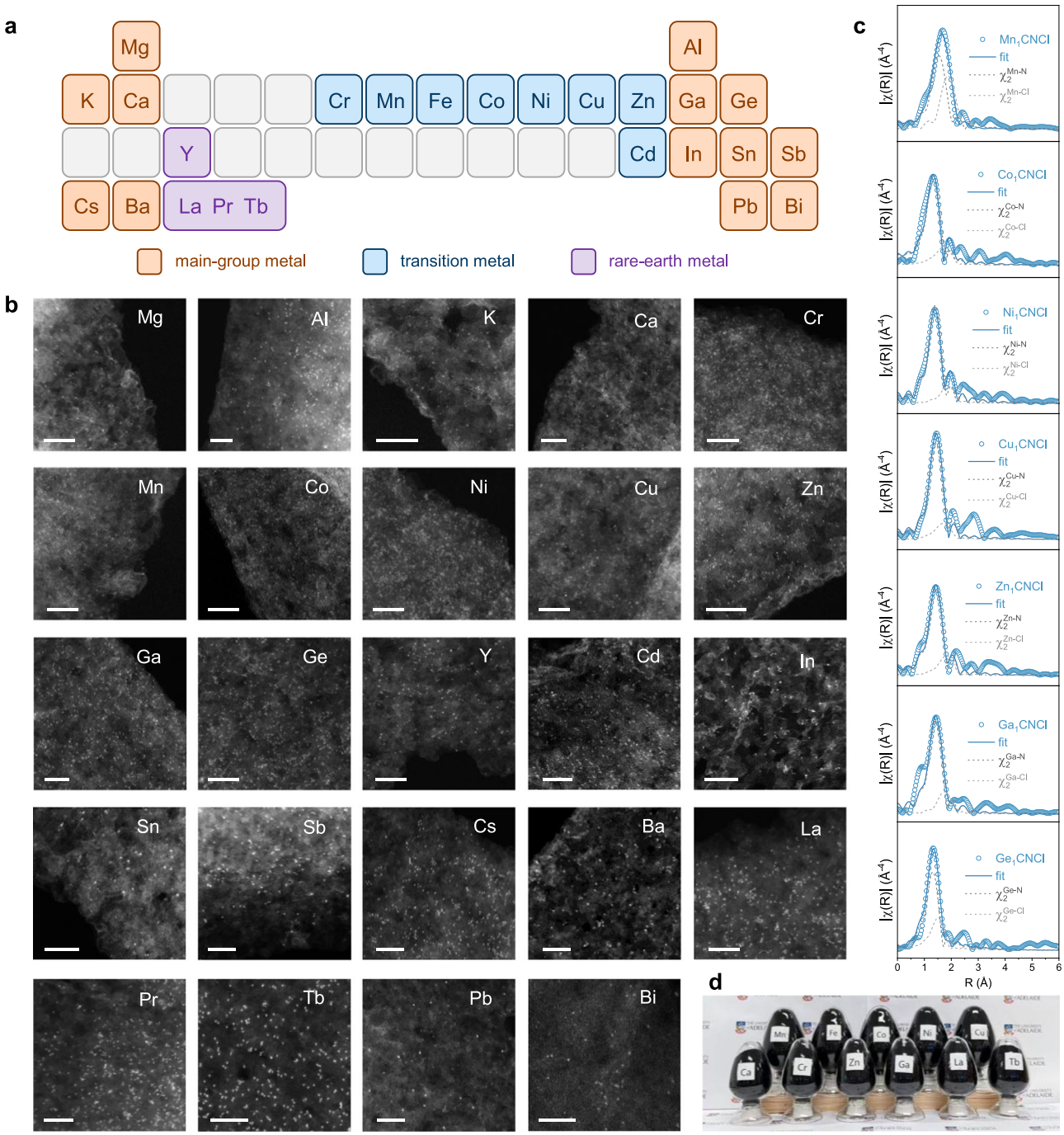

Fig. 3 | Synthesis of different SACs. a Schematic diagram of a SAC library. The orange, blue and purple boxes represent the main group, transition and rare earth metals, respectively. **b** HAADF-STEM images of 24 SACs. The scale bar is 5 nm. **c** The FT-EXAFS analysis for M_1CNCl fits in R space. **d** Photographs of batches containing 10 g of Mn, Fe, Co, Ni, Cu and 5 g of Ca, Cr, Zn, Ga, La, Tb SACs.

XRD analyses show no reflection corresponding to bulk metal or metal oxides (Supplementary Figs. 15–38), but the characteristic diffraction peaks of carbon support, confirming the atomic-scale metal dispersion. HAADF-STEM images provide a direct evidence of atomic dispersion (Fig. 3b), showing bright, well-dispersed atomic sites on the carbon support without visible clusters or nanoparticles. EDS mapping further confirms the uniform distribution of metal atoms along with C, N and Cl (Supplementary Figs. 15–38).

To gain deeper insights into the coordination environment, we conducted EXAFS analysis to investigate representative samples, containing Mn, Co, Ni, Cu, Zn, Ga, and Ge (Supplementary Figs. 20–26). Their respective FT-EXAFS spectra reveal the absence of characteristic metal-metal bonds typically observed in their corresponding metal foils, corroborating the atomic dispersion as revealed by HAADF-STEM. Additionally, EXAFS fitting of the R-space reveals that different single atoms exhibit the same coordination mode of Cl_1–M–N_4 (Fig. 3c and Supplementary Table 2), confirming a universal guiding principle of axially engineering for SACs enabled by the molten NaCl template.

To further assess the efficiency of this synthesis method, we analyzed the mass yield across various metal SACs (Supplementary Fig. 39). Mn_1CNCl exhibited the lowest yield at 18.3%, while Sb_1CNCl had the highest yield at 50.9%. Despite this variation, the overall average mass yield for the 25 metals was 30.5%, demonstrating the effectiveness and reliability of the method across a broad range of

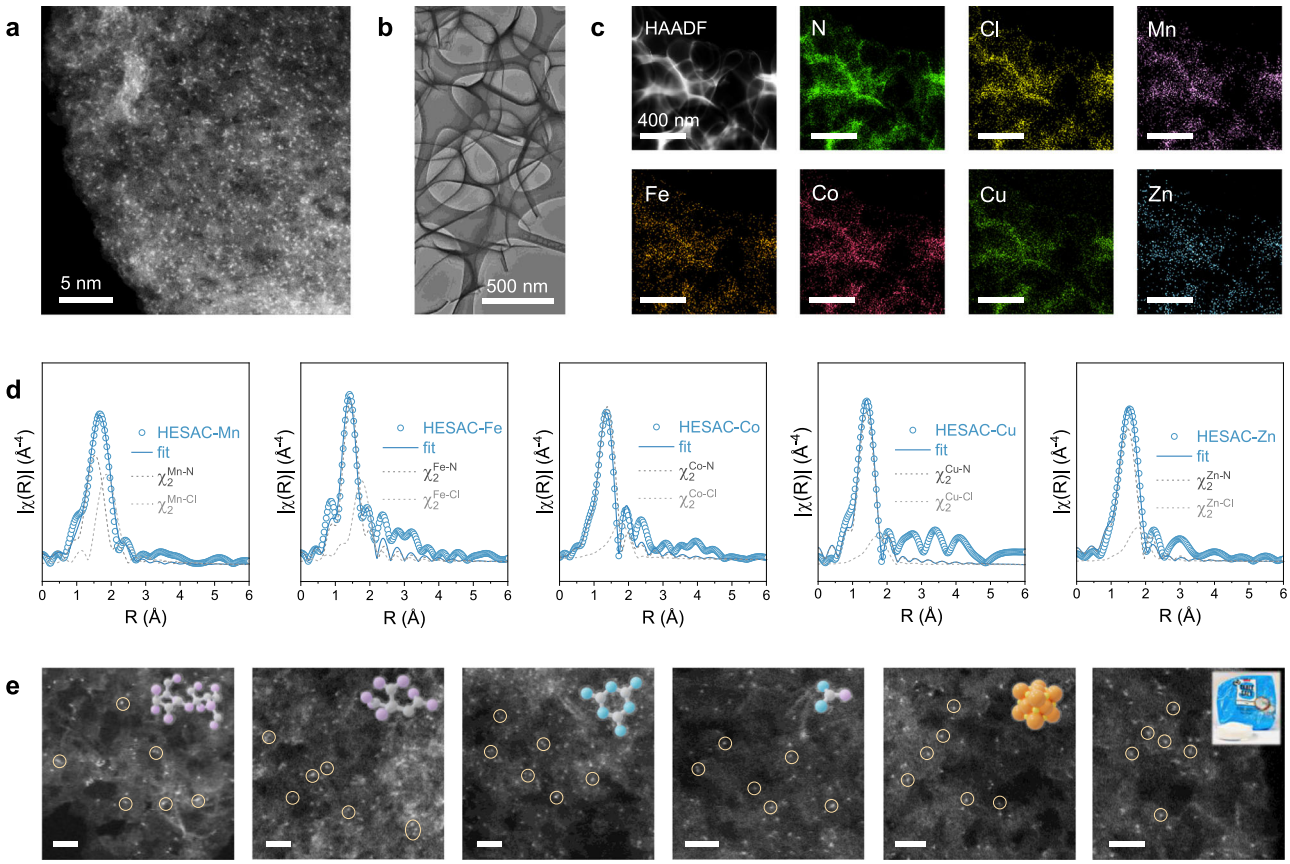

Fig. 4 | Synthesis of MnFeCoCuZn-HESACs. a HAADF-STEM, **b** TEM image of HESACs and **c** corresponding EDS mappings of N, Cl, Mn, Fe, Co, Cu and Zn (The scale bar is 400 nm). **d** FT-EXAFS spectra of the metals in HESACs. **e** HAADF-STEM images of Fe SACs synthesized via an alternate component (The scale bar is 2 nm). The inset images correspond to the following replacement components: sucrose, citric acid, melamine, urea, potassium chloride, and commercial table salt, respectively. Gray sphere: C; purple sphere: O, blue sphere: N; orange sphere: K; yellow sphere: Cl.

metals. The high product yield is attributed to the confined catalytic graphitization of precursors between the NaCl grain boundaries, which significantly reduces the precursor (and decomposed intermediate) volatilization and SAC decomposition losses. Leveraging this high yield, we successfully produced gram-scale SACs (Fig. 3d), highlighting the scalability of the method for practical production and applications.

Moreover, we successfully extended this method to synthesize multi-metal HESACs, containing Mn, Fe, Co, Cu, and Zn on the carbon support, overcoming the aggregations not only among identical metals but also across different metallic species (Supplementary Fig. 40). The HAADF-STEM image and EDS element mapping exhibit uniform dispersion of all five metals across the carbon support, and TEM image confirms the similar 3D honeycomb structure (Fig. 4a–c). The positive oxidation states of the metal sites are confirmed by corresponding XANES (Supplementary Fig. 40). The absence of the metal–metal path between 2.0 and 2.5 Å in FT-EXAFS (Fig. 4d) and the lack of corresponding WT-EXAFS signal at r > 2.0 Å in WT-EXAFS confirm that all metal sites remain atomically isolated (Supplementary Fig. 41). The FT-EXAFS fitting results indicate that all five metals have a moiety of Cl_1–M–N_4 (Fig. 4d and Supplementary Table 3). Therefore, this work also provides a universal synthetic strategy to fabricate various well-defined HESACs.

In addition, this strategy can be adapted using alternative carbon precursors (e.g., citric acid and sucrose) and nitrogen sources (e.g., melamine and urea), as well as different salt templates (e.g., potassium chloride and commercial table salt), to achieve single-atom dispersion on carbon (Fig. 4e and Supplementary Figs. 42–47). Moreover, it also exhibits compatibility with secondary coordination sphere modulation, as demonstrated in our recent work on multidimensional engineering of Co sites with second-shell S atoms[4], further confirming its versatility in constructing diverse and well-defined M_1CNCl catalysts.

Catalytic applications

The catalytic performance of these newly developed SACs was firstly evaluated in the Fenton-like reaction for catalytic degradation of a pharmaceutical pollutant-sulfamethoxazole (SMX) with PMS (Supplementary Fig. 48–51). The metal-free catalyst (CN) exhibited limited efficacy in PMS activation (Supplementary Fig. 52), achieving only 34% of SMX removal within 10 min. Figure 5a shows the rate constants (k_{obs}) of different SACs. Among them, Fe_1CNCl exhibited the highest catalytic activity, achieving a complete SMX removal in just 3 min, with a k_{obs} at 35.6 times higher than CN. Notably, Fe_1CNCl demonstrated substantially higher activity than its Cl-free counterpart Fe_1CN (Supplementary Fig. 53). This exceptional catalytic performance can be attributed to the unique axial coordination of Fe, which modulates its electronic properties and enhances the reactivity toward PMS activation[28]. Considering that k_{obs} can be affected by reaction conditions, a normalized kinetic model (k-n), accounting for catalyst loading, oxidant and pollutant concentrations, was employed to provide a fair comparison across different heterogeneous Fenton-like systems. Under this metric, Fe_1CNCl outperformed most state-of-the-art catalysts in PMS-based oxidation reported to date, including carbon-supported metal nanoparticles and other SACs (Fig. 5b and Supplementary Table 4)[29–37]. Based on controlled quenching experiments, chemical probes, electron paramagnetic resonance (EPR) and open-circuit potential (OCP) tests (Supplementary Figs. 54–58), the exceptional catalytic activity of the

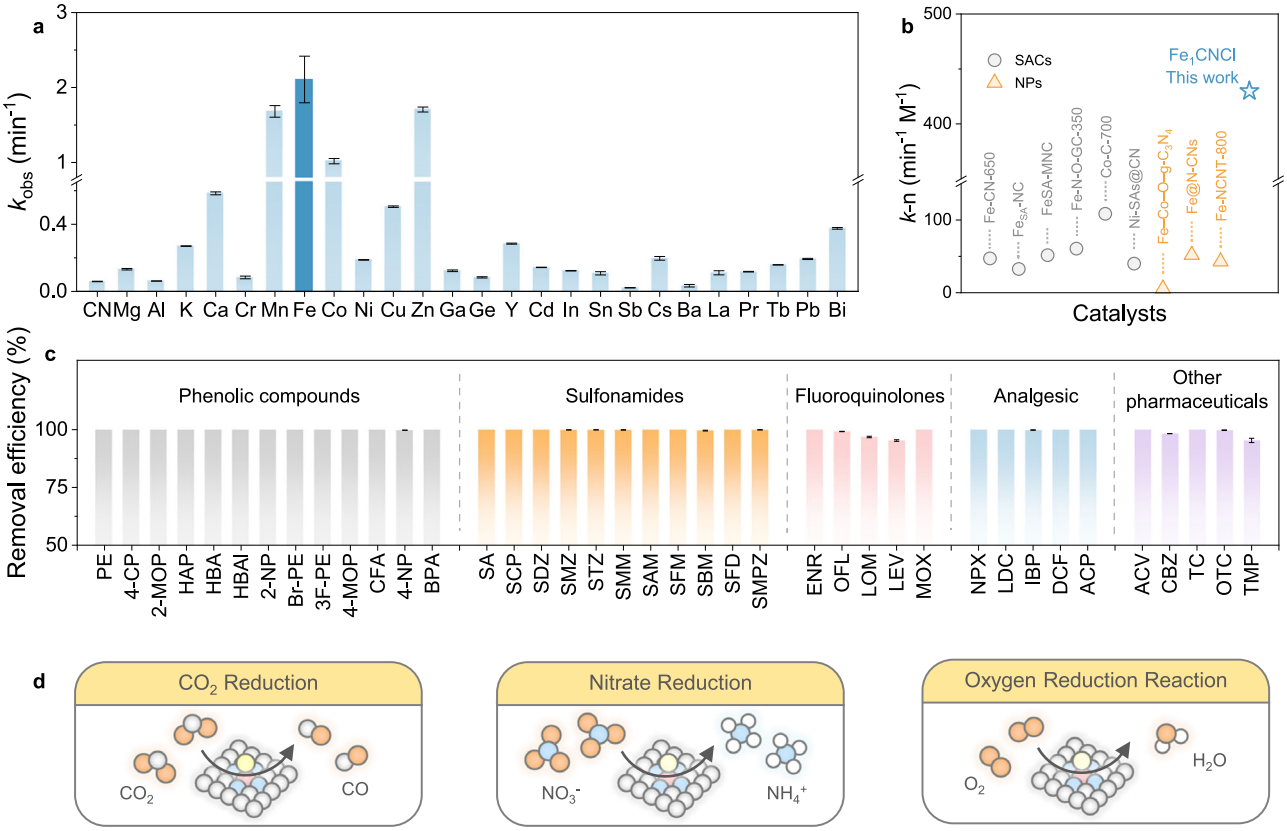

Fig. 5 | Catalytic applications of catalysts. a k_{obs} of SMX removal by M_1CNCl catalysts. **b** Comparison of *k*-n for the state-of-the-art heterogeneous Fenton-like catalysts. **c** Removal efficiency of pharmaceutical and phenolic pollutants (0.02 mM) in the Fe_1CNCl/PMS system. Experimental conditions: [SMX] = 0.02 mM, [PMS] = 0.5 mM, [catalyst] = 0.05 g L^{-1}. **d** Schematics of SACs for other catalytic reduction reactions. Error bars represent the standard deviations by repeating the experiment twice.

Fe_1CNCl/PMS system can be attributed to the synergistic mechanism of high-valent iron-oxo species (HVI) and electron transfer processes mediated by the Fe_1CNCl − PMS* complex. These factors together facilitate efficient pollutant degradation via nonradical oxidation.

We further evaluated the practical effectiveness of the Fe_1CNCl/PMS system for pollutant removal considering background factors in real wastewater. The system exhibited robust resistance to interference from co-existing ions, including representative cations (Ca^{2+}, Mg^{2+}) and anions (Cl^-, NO_3^-, $H_2PO_4^-$) (Supplementary Fig. 59). Furthermore, the system maintained high catalytic activity over a broad pH range (3–9), achieving 100% SMX degradation within 10 min (Supplementary Fig. 60). Only trace amounts of Fe leaching were detected after the reaction, confirming a negligible contribution to PMS activation and minimal risk of secondary contamination (Supplementary Fig. 61). Post-reaction characterizations further confirmed that the morphology and structure of Fe_1CNCl were well preserved (Supplementary Fig. 62). Moreover, SMX removal efficiency was evaluated in various water matrices, including ultrapure water, tap water, river water (Torrens River), simulated urine and seawater (Glenelg beach), and demonstrated consistently high removal values (>89%) in all the cases (Supplementary Fig. 63). These findings highlight the versatility and stability of the Fe_1CNCl catalyst in real-world remediation tasks.

With the growing concerns over emerging contaminants in aquatic environments, we extended the assessment of Fe_1CNCl/PMS against a broader range of pollutants. As a result, this nonradical oxidative system can effectively remove 39 diverse pollutants (Fig. 5c, Supplementary Fig. 64 and Table 5), including thirteen phenolic compounds, eleven sulfonamide antibiotics, five quinolone antibiotics, five analgesics, and other five kinds of pharmaceutical contaminants, achieving over 95% removal within 10 min, demonstrating its broad applicability and high efficiency in tackling complex wastewater contaminants. Additionally, Fe_1CNCl demonstrated universal activation capability toward different oxidants, including persulfate (PDS), periodate (PI) and peracetic acid (PAA) (Supplementary Fig. 65). These findings collectively highlight the adaptability and promise of Fe_1CNCl for complex water treatment scenarios.

Additionally, we explored M_1CNCl in electrocatalytic processes for chemical synthesis and energy conversion (Fig. 5d), such as nitrate reduction reaction to ammonia (NO_3^-RR, Supplementary Figs. 66–68), CO_2 reduction reaction to CO (CO_2RR, Supplementary Figs. 69–70) and oxygen reduction reaction (ORR, Supplementary Fig. S71). Fe_1CNCl achieved higher current densities and significantly improved ammonia yields across all tested potentials compared to CN, delivering an ~3.3-fold improvement over the metal-free counterpart at −1.6 V vs. Ag/AgCl (Supplementary Figs. 66–68). Additionally, CO_2RR performance for the M_1CNCl catalysts was directly evaluated via electrolyzing at specified currents (Supplementary Figs. 69–70). Ni_1CNCl exhibited a high CO_2-to-CO conversion efficiency in a broad current density of 10–200 mA cm^{-1}, with a maximum FE of 97.4% at 200 mA cm^{-1}, comparable to or surpassing reported Ni SACs (Supplementary Table 6). In the ORR measurements (Supplementary Fig. 71), $Ni_1/Fe_1/Co_1$CNCl exhibit an enhanced four-electron pathway to convert oxygen into water. These findings demonstrate that NaCl-assisted M_1CNCl catalysts offer versatile approaches for tackling key environmental and sustainable issues, underlining their broad applicability.

Discussion

In summary, we developed a facile and scalable NaCl-templating method for massive production of a comprehensive library of SACs

with precise coordination structures. Ex-situ characterizations, combined with DFT calculations, revealed a temperature-driven metal coordination transformation during the annealing process. A low-cost and recyclable NaCl template acted as both a morphology-directing and coordination-controlling agent. This process led to the formation of a 3D honeycomb-like structure, with lower temperatures favoring in-plane M–N_x ($x = 4$ or 6) coordination, while higher temperatures around 900 °C led to axial M–Cl coordination through ion dissociation from the molten salt. This approach has enabled the successful synthesis of 25 distinct SACs as well as HESACs containing five different metal atoms. Moreover, the outstanding catalytic activity of Fe_1CNCl was demonstrated in PMS-based pollutant oxidation in a selective nonradical manner. The broad applicability of these SACs was also validated in various electrocatalytic reduction reactions for chemical synthesis and energy conversion. This NaCl-assisted synthesis method not only offers a robust platform for the precise design of SAC materials and mass production but also underscores its potential for diverse environmental and sustainable catalysis.

Methods

Preparation of M_1CNCl catalysts

A mixture consisting of 3 g of NaCl, 300 mg of glucose, 0.1 mmol of metal chlorides or nitrates, and 400 mg of dicyandiamide was dissolved in 30 mL of deionized water. The solution was freeze-dried under vacuum to obtain a solid powder, which was then pyrolyzed for 2 h at 900 °C in an argon atmosphere, with a heating rate of 5 °C/min. After cooling to room temperature, the resulting black powder was treated with 0.5 M H_2SO_4. The treated powder was dried at 60 °C and was referred to as M_1CNCl. The synthesis process can be proportionally scaled up to produce larger quantities of the catalyst. For the synthesis of the nitrogen-doped carbon catalyst (CN), the same procedure was followed, excluding the addition of metal salts. Detailed methods for other comparison samples are provided in the Supplementary Information.

Characterizations. X-ray powder diffraction (XRD) patterns were acquired using a Rigaku MiniFlex 600 X-ray diffractometer. SEM images were captured with a FEI Quanta 450 FEG Environmental Scanning Electron Microscope. TEM images were obtained using an FEI Tecnai G2 Spirit TEM. High angle annular dark-field scanning TEM (HAADF-STEM) images along with EDS analysis were performed on an FEI Titan Themis 80-200 operating at 200 kV. XAS analysis was conducted under ambient conditions. Metal foils and metal oxides were regarded as the standard references. Both XANES and EXAFS spectra were obtained at the Australian Synchrotron in Melbourne. All the spectra data were processed and analyzed using the QANT software program and ATHENA/ARTEMIS module of IFEFFIT software package[38,39].

Fenton-like reaction

In a temperature-controlled water bath set at 25 °C, a catalyst concentration of 0.05 g/L and 0.5 mM PMS were added to 50 mL of a 0.02 mM SMX solution. The pH was modified using sulfuric acid (H_2SO_4) and sodium hydroxide (NaOH). Samples were periodically collected using a syringe and immediately filtered through a 0.22 μm polyether sulfone membrane. Each 1 mL sample was mixed with 20 μL of sodium thiosulfate solution before being transferred into vials for high-performance liquid chromatography (HPLC) analysis. The detection of pollutants was performed using an ultrahigh-performance liquid chromatography (UHPLC) system from Thermo Scientific, equipped with a C-18 column and a UV detection system.

Data availability

The data supporting the findings of the study are included in the main text and supplementary information files. Additional data can be obtained from the corresponding author upon request. Source data are provided with this paper.

References

1. Guo, J. et al. Size-dependent catalysis in Fenton-like chemistry: from nanoparticles to single atoms. *Adv. Mater.* **36**, e2403965 (2024).
2. Duan, Y. et al. Large-scale synthesis of high-loading single metallic atom catalysts by a metal coordination route. *Adv. Mater.* **36**, e2404900 (2024).
3. Zhu, Z. S. et al. Microenvironment engineering of heterogeneous catalysts for liquid-phase environmental catalysis. *Chem. Rev.* **124**, 11348–11434 (2024).
4. Zhu, Z.-S. et al. Multidimensional engineering of single-atom cobalt catalysts for ultrafast Fenton-like reactions. *Nat. Water* **3**, 211–221 (2025).
5. Zhu, Z. S. et al. Atomic-level engineered cobalt catalysts for Fenton-like reactions: synergy of single atom metal sites and nonmetal-bonded functionalities. *Adv. Mater.* **36**, e2401454 (2024).
6. Li, G. et al. Dimensionality engineering of single-atom nanozyme for efficient peroxidase-mimicking. *J. Am. Chem. Soc.* **145**, 16835–16842 (2023).
7. Huang, T. et al. Coordination environment-tailored electronic structure of single atomic copper sites for efficient electrochemical nitrate reduction toward ammonia. *Energy Environ. Sci.* **17**, 8360–8367 (2024).
8. Yang, H. et al. Scalable production of efficient single-atom copper decorated carbon membranes for CO_2 electroreduction to methanol. *J. Am. Chem. Soc.* **141**, 12717–12723 (2019).
9. Han, L. et al. A single-atom library for guided monometallic and concentration-complex multimetallic designs. *Nat. Mater.* **21**, 681–688 (2022).
10. He, X. et al. A versatile route to fabricate single atom catalysts with high chemoselectivity and regioselectivity in hydrogenation. *Nat. Commun.* **10**, 3663 (2019).
11. Liu, X. et al. Double bonuses achieved in single-atom catalysts for efficient oxygen evolution: enhanced reaction kinetics and reinforced electrochemical reconstruction. *Adv. Funct. Mater.* **34**, 2309824 (2023).
12. Xie, F. et al. A general approach to 3D-printed single-atom catalysts. *Nat. Synth.* **2**, 129–139 (2023).
13. Ji, S. et al. Chemical synthesis of single atomic site catalysts. *Chem. Rev.* **120**, 11900–11955 (2020).
14. Guo, W., Wang, Z., Wang, X. & Wu, Y. General design concept for single-atom catalysts toward heterogeneous catalysis. *Adv. Mater.* **33**, e2004287 (2021).
15. Li, Z. et al. Iridium single-atom catalyst on nitrogen-doped carbon for formic acid oxidation synthesized using a general host-guest strategy. *Nat. Chem.* **12**, 764–772 (2020).
16. Lai, W. H. et al. General synthesis of single-atom catalysts for hydrogen evolution reactions and room-temperature Na-S batteries. *Angew. Chem. Int. Ed.* **59**, 22171–22178 (2020).
17. Liu, W. et al. Discriminating catalytically active FeN_x species of atomically dispersed Fe-N-C catalyst for selective oxidation of the C-H bond. *J. Am. Chem. Soc.* **139**, 10790–10798 (2017).
18. Li, H., Pan, F., Qin, C., Wang, T. & Chen, K. J. Porous organic polymers-based single-atom catalysts for sustainable energy-related electrocatalysis. *Adv. Energy Mater.* **13**, 2301378 (2023).
19. Jiao, L. et al. Nanocasting SiO_2 into metal-organic frameworks imparts dual protection to high-loading Fe single-atom electrocatalysts. *Nat. Commun.* **11**, 2831 (2020).
20. Hu, C. et al. Hierarchically ordered pore engineering of carbon supports with high-density edge-type single-atom sites to boost electrochemical CO_2 reduction. *Adv. Mater.* **36**, e2409531 (2024).

21. Wu, Z.-Y. et al. A general synthesis of single atom catalysts with controllable atomic and mesoporous structures. *Nat. Synth.* **1**, 658–667 (2022).
22. Zhang, Y. et al. Nanostructured single-atom catalysts derived from natural building blocks. *EES Catal.* **2**, 475–506 (2024).
23. Hu, L. et al. Metal-triazolate-framework-derived FeN_4Cl_1 single-atom catalysts with hierarchical porosity for the oxygen reduction reaction. *Angew. Chem. Int. Ed.* **60**, 27324–27329 (2021).
24. Zhang, X. et al. Atomically dispersed hierarchically ordered porous Fe–N–C electrocatalyst for high performance electrocatalytic oxygen reduction in Zn-Air battery. *Nano Energy* **71**, 104547 (2020).
25. Wei, S. et al. Axial chlorination engineering of single-atom nanozyme: Fe-N_4Cl catalytic sites for efficient peroxidase-mimicking. *J. Am. Chem. Soc.* **146**, 33239–33248 (2024).
26. Wu, Z. et al. Long-range interactions driving neighboring Fe-N_4 sites in Fenton-like reactions for sustainable water decontamination. *Nat. Commun.* **15**, 7775 (2024).
27. Guo, J. et al. Fenton-like activity and pathway modulation via single-atom sites and pollutants comediates the electron transfer process. *Proc. Natl. Acad. Sci. USA* **121**, e2313387121 (2024).
28. Ren, S. et al. Transforming plastics to single atom catalysts for peroxymonosulfate activation: axial chloride coordination intensified electron transfer pathway. *Adv. Mater.* **37**, e2415339 (2025).
29. He, J. et al. The enhanced catalytic degradation of sulfamethoxazole over Fe@nitrogen-doped carbon-supported nanocomposite: insight into the mechanism. *Chem. Eng. J.* **439**, 135784 (2022).
30. Huang, B. et al. Coupled surface-confinement effect and pore engineering in a single-Fe-atom catalyst for ultrafast Fenton-like reaction with high-valent iron-oxo complex oxidation. *Environ. Sci. Technol.* **57**, 15667–15679 (2023).
31. Song, W., Xiao, X., Wang, G., Dong, X. & Zhang, X. Highly efficient peroxymonosulfate activation on Fe-N-C catalyst via the collaboration of low-coordinated Fe-N structure and Fe nanoparticles for enhanced organic pollutant degradation. *J. Hazard. Mater.* **455**, 131596 (2023).
32. Wang, S., Liu, Y. & Wang, J. Peroxymonosulfate activation by Fe-Co-O-codoped graphite carbon nitride for degradation of sulfamethoxazole. *Environ. Sci. Technol.* **54**, 10361–10369 (2020).
33. Wang, S. & Wang, J. Single atom cobalt catalyst derived from co-pyrolysis of vitamin B_{12} and graphitic carbon nitride for PMS activation to degrade emerging pollutants. *Appl. Catal. B* **321**, 122051 (2023).
34. Wang, S., Xu, L. & Wang, J. Iron-based dual active site-mediated peroxymonosulfate activation for the degradation of emerging organic pollutants. *Environ. Sci. Technol.* **55**, 15412–15422 (2021).
35. Yang, J. et al. Insights into the role of dual reaction sites for single Ni atom Fenton-like catalyst towards degradation of various organic contaminants. *J. Hazard. Mater.* **430**, 128463 (2022).
36. Zeng, Y. et al. Mediated peroxymonosulfate activation at the single atom Fe-N_3O_1 sites: synergistic degradation of antibiotics by two non-radical pathways. *Small* **20**, e2311552 (2024).
37. An, S., Yang, J. & Jin, Q. Highly efficient peroxymonosulfate activation of single-atom Fe catalysts via integration with Fe ultrafine atomic clusters for the degradation of organic contaminants. *Sep. Purif. Technol.* **300**, 121910 (2022).
38. Gann, E., McNeill, C. R., Tadich, A., Cowie, B. C. C. & Thomsen, L. Quick AS NEXAFS Tool (QANT): a program for NEXAFS loading and analysis developed at the Australian Synchrotron. *J. Synchrotron Radiat.* **23**, 374–380 (2016).
39. Ravel, B. & Newville, M. ATHENA, ARTEMIS, HEPHAESTUS: data analysis for X-ray absorption spectroscopy using IFEFFIT. *J. Synchrotron Radiat.* **12**, 537–541 (2005).

Acknowledgements

The authors acknowledge the financial support from the Australian Research Council (FT230100526 to X.D., FL230100178 to S.W. and DP230102406 to X.D.). Part of this research was undertaken on the X-ray Absorption Spectroscopy, Medium Energy X-ray Absorption Spectroscopy and Soft X-ray Spectroscopy beamlines at the Australian Synchrotron, part of ANSTO.

Author contributions

Z.-S.Z. and X.D. designed research. Z.-S.Z. carried out the experiments and wrote the manuscript. H.L. finished the DFT calculation section. P.W. and Y.W. assisted to run catalytic tests. Y.L., K.H., B.J., S.R. and S.Z. assisted to performed characterizations. P.W., X.D. and S.W. further revised the manuscript. H.S., X.D. and S.W. supervised the project. All authors discussed the results and commented on the manuscript.

Competing interests

The authors declare no competing interests.

Additional information

Supplementary information The online version contains supplementary material available at https://doi.org/10.1038/s41467-025-63117-7.

Correspondence and requests for materials should be addressed to Xiaoguang Duan or Shaobin Wang.

Peer review information *Nature Communications* thanks the anonymous reviewers for their contribution to the peer review of this work. A peer review file is available.